EPJ Photovoltaics **11**, 7 (2020)

https://doi.org/10.1051/epjpv/2020004

Available online at:
www.epj-pv.org

REGULAR ARTICLE OPEN ACCESS

Solution-processed TiO_2 as a hole blocking layer in PEDOT:PSS/n-Si heterojunction solar cells

Md. Enamul Karim, A.T.M. Saiful Islam*, Yuki Nasuno, Abdul Kuddus, Ryo Ishikawa, and Hajime Shirai

Graduate School of Science and Engineering, Saitama University, Saitama 338-8570, Japan

Received: 11 September 2019 / Received in final form: 15 January 2020 / Accepted: 7 April 2020

Abstract. The junction properties at the solution-processed titanium dioxide (TiO_2)/n-type crystalline Si(n-Si) interface were studied for poly(3,4-ethylenedioxythiophene):poly(styrene sulfonate) (PEDOT:PSS)/n-Si heterojunction solar cells by the steady-state photovoltaic performance and transient reverse recovery characterizations. The power conversion efficiency could be increased from 11.23% to 13.08% by adjusting the layer thickness of TiO_2 together with increasing open-circuit voltage and suppressed dark saturation current density. These findings originate from the enhancement of the carrier collection efficiency at the n-Si/cathode interface. The transient reverse recovery characterization revealed that the surface recombination velocity S was ~375 cm/s for double TiO_2 interlayer of ~2 nm thickness. This value was almost the same as that determined by microwave photoconductance decay measurement. These findings suggest that solution-processed TiO_2 has potential as a hole blocking layer for the crystalline Si photovoltaics.

Keywords: Hole blocking layer / TiO_2 / surface recombination velocity / transient reverse recovery

1 Introduction

Carrier selective layers using metal oxides and organic materials for crystalline Si (c-Si) photovoltaics have been extensively studied to replace classical high-temperature p-n junction and low-pressure processing. They include aluminum oxide (Al_2O_3), NiO, graphene oxide, and the transparent conductive polymer poly(3,4-ethylenedioxythiophene): poly(styrene sulfonate) (PEDOT:PSS) as an electron blocking layer (EBL). Among them, solution-processed PEDOT:PSS provides good passivation of c-Si and acts as a transparent hole transporting layer, which induces strong inversion at the PEDOT:PSS/n-Si interface without any additional impurity doping. The junction properties at PEDOT:PSS/n-Si interfaces can be explained in terms of p^+-n junction model [1–3]. However, the band bending at the rear cathode interface is still less than the anode interface despite the use of a low work function metal [4–6]. To address this, several interfacial materials which act as an electron selective layer (ESL) have been studied, including transition metal oxides and fluorinated alkali metals such as magnesium oxide (MgO) [7], titanium oxide (TiO_2) [8–13], barium hydroxide ($Ba(OH)_2$) [14,15], cesium carbonate (Cs_2CO_3) [16,17], lithium fluoride (LiF) [18,19], magnesium fluoride (MgF_2) [20]. Among them, TiO_2 on Si (100) has been shown to blocks holes ($\Delta E_V \geq 2.3$ eV) while being transparent to electrons ($\Delta E_C < 0.3$ eV), thereby acting as a hole blocking layer (HBLs). Several deposition methods have been applied for the fabrication of TiO_2 thin films such as PE-CVD [21–24], metal-organic chemical vapor deposition (MO-CVD) [25], pulsed laser deposition (PLD) [26], atomic layer deposition (ALD) [27–30], sputtering [31], and sol-gel [32]. Among them, ALD of TiO_2 has been extensively studied and effective minority carrier recombination velocities below 100 cm/s have been achieved [33]. However, the potential of solution-processed TiO_2 as an HBL for n-Si heterojunction solar cells is still not clear.

The present study demonstrates the potential of solution-processed TiO_2 as an HBL to improve the photovoltaic performance of PEDOT:PSS/n-Si/TiO_2 double heterojunction solar cells. The junction properties of n-Si/TiO_2 cathode interfaces are also investigated in terms by transient reverse recovery T_{rr} measurement to determine the effective surface recombination velocity S at n-Si/TiO_2 interface.

2 Experimental procedure

2.1 Solution-processed TiO_2 and device fabrication

Figure 1 shows the molecular structure of PEDOT:PSS and device structure of PEDOT:PSS/n-Si/TiO_2 double heterojunction solar cells. Both-side-polished 2×2-cm^2 n-type

* e-mail: saifulslm6@gmail.com

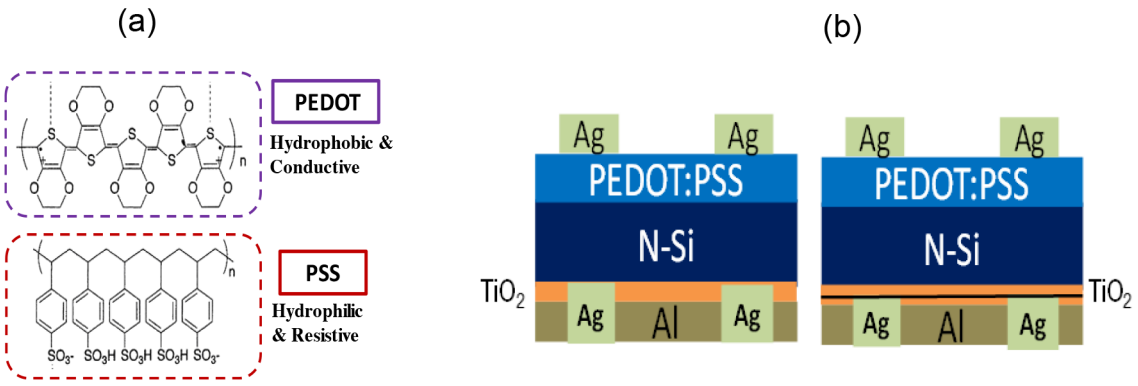

Fig. 1. (a) Molecular structure of PEDOT:PSS, (b) schematic of PEDOT:PSS/n-Si/TiO_2 double heterojunction solar cells with single- and double-TiO_2 layers as an HBL.

(100) CZ c-Si wafers (1–5 Ω cm) with a thickness of 250 μm were used as the base substrate. Prior to the film deposition, the n-Si substrates were ultrasonically cleaned with acetone, isopropanol, and DI-water for 10 min each, followed by 5 wt.% HF_{aq} treatment for 3 min to remove the native oxide. As a first step, a solution of PEDOT:PSS (prepared from Clevios^R PH1000 by adding ethylene-glycol and capstone fluorosurfactant in a ratio of 93:7:0.16 wt.%) was spin-coated (SC) on top of the cleaned n-Si substrate, followed by thermal annealing at 140 °C for 30 min to remove the residual solvent. Then Ag grid electrodes were screen printed at the top of the PEDOT:PSS. In a next step, a precursor solution of titanium tetraisopropoxide [Ti$(OCH(CH_3)_2]_4$:TiP) diluted in isopropyl alcohol at three different concentrations of 0.5, 1, and 2 mg/ml was spin-coated at 3000 rpm for 40 s on the rear side of the n-Si followed by thermal annealing at 140 °C for 10 min to remove the residual solvent. The hydrolysis reaction described below was applied to synthesize titanium dioxide on the n-Si substrate as an HBL [34].

$$Ti\{OCH(CH_3)_2\}_4 + 2H_2O \rightarrow TiO_2 + 4(CH_3)_2CHOH.$$

Two types of device structures were fabricated as shown in Figure 1b. One is a single layer of PEDOT:PSS (80 nm)/n-Si/TiO_2 double heterojunction solar cells of 1, 2, and 3 nm thickness TiO_2, formed by adjusting the solution concentration on the top of the Ag grid electrode, to understand the thickness effect of TiO_2 on cathode interface. The other is the alternate coating of TiO_2 layers to suppress the junction area at the Ag/n-Si contact. This structure was fabricated by first forming a 1-nm-thick TiO_2 layer on the n-Si substrate, followed by a screen print of the Ag grid electrode. Then, another 2-nm-thick TiO_2 was spin coated on top of the Ag grid/TiO_2/n-Si structure. Finally, the Al was evaporated in from the entire area of the rear side to form the cathode electrode.

2.2 Characterizations

The junction properties at the TiO_2/n-Si interface were evaluated using atomic force microscopy (AFM), X-ray photoemission spectroscopy (XPS), effective minority carrier lifetime τ_{eff}, and the electroluminescence in solar cell under dark current injection in the forward bias condition.

2.2.1 XPS study

XPS measurements were performed for the Ti^{4+} peak with a binding energy of 458.6 eV for $2p_{3/2}$ and 464.7 eV for $2p_{1/2}$ and the Si(2p) line region at 99.4 ± 0.3 eV using a monochromatized Al K_α radiation of $h\nu = 1486.6$ eV [AXIS-Nova (Kratos Analytical)]. The formation of suboxides at the TiO_2/n-Si interface was examined by deconvolution including metallic Si, Si^+, Si^{2+} and Si^{4+} complexes in the 100–104 eV regions. The effect of Al metallization on the Al/TiO_2/n-Si interface was examined by depositing Al a few nanometers thick by evaporation.

2.2.2 Carrier lifetime

The PEDOT:PSS and TiO_2 layers on n-Si n-type c-Si(1-5 Ω · cm) substrates were examined through a 2D map of minority carrier lifetime τ_{eff} measurements (SLT-1410A, KOBELCO). TiO_2 layers with different thicknesses were spin coated by adjusting the solution concentration and then thermally annealed at 140 °C for 10 min prior to the lifetime measurement.

2.2.3 Characterization of solar cells

The current density–voltage (J–V) characteristics were measured in the dark and under exposure with simulated solar light of AM1.5G, 100 mW/cm^2 [Bunkoukeiki (CEP-25BX)]. The light exposure area was masked using a shadow mask to avoid the light leakage. The photovoltaic performance was studied using a 2 × 2-cm^2 device under simulated of AM1.5 solar light exposure at 25 °C. The short-circuit current density J_{sc}, open-circuit voltage V_{oc}, fill factor FF and power conversion efficiency PCE were determined from the photocurrent density–voltage (J–V) curves. The external quantum efficiency EQE was also measured with and without bias light exposure. The two-dimensional (2D) map of EQE at 1000 nm was also characterized for devices with a 2 × 2 cm^2 area using a Lasertec: MP Series.

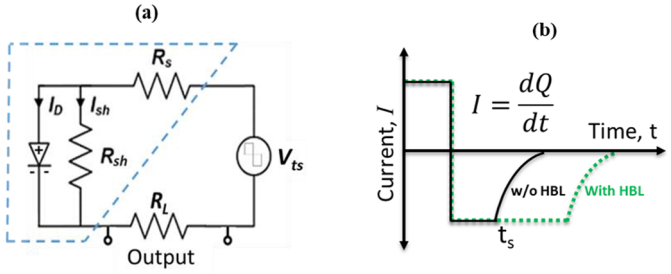

Fig. 2. Schematics of (a) the circuit diagram and (b) T_{rr} current for devices with and without HBLs.

2.2.4 Transient reverse recovery T_{rr} measurement

T_{rr}, unlike μ-PCD, does not is need to use both sides of the symmetric TiO_2 coated samples to determine S. Hence, it can be used to determine the recombination velocity of the complete solar cell device structure. Figure 2 presents (a) the circuit diagram used for the T_{rr} study and (b) the expected output current. Here, V_{ts} is the transient bias source, R_L (100 Ω) is the external load resistance, the blue dashed line area represents the simple equivalent circuit of the solar cell device, and R_s and R_{sh} are equivalent series and shunt resistance. The details of the T_{rr} measurement are described in references [35,36]. First, a positive V_{ts} higher than the built-in potential is applied to the circuit to achieve the steady forward current level I_D and I_{sh}. Then, a reverse bias is applied to the device under test and the time of recovery to a steady state was monitored by combining a programmable rectangle wave (WW2074 model of Tabor Electronics) of 1 KHz and the digital storage oscilloscope (DSO7054A model of Agilent Technologies) signal. The amount of stored charge inside the bulk can be calculated by:

$$Q = It_s \tag{1}$$

where, I is the maximum recovery current and t_s is the storage time. Assuming that $I_{si/HBL}$ ($t_{si/HBL}$) and I_{si} (t_{si}) are the transient currents (storage times) for devices with and without HBLs, then the storage charge ratio Q_{ratio} can be determined by:

$$Q_{ratio} = \frac{Q_{Si/HBL}}{Q_{Si}} = \frac{I_{Si/HBL}t_{Si/HBL}}{I_{Si}t_{Si}} \tag{2}$$

$$\text{If,} \quad I_{Si/HBL} \approx I_{Si}, \quad Q_{ratio} = \frac{t_{Si/HBL}}{t_{Si}} \tag{3}$$

Q_{ratio} can be obtained from the diffusion coefficient D_p and recombination velocity S as follows:

$$Q_{ratio} = 2\frac{D_p}{WS} + 1$$

$$S = \frac{2D_p}{W(Q_{ratio} - 1)}. \tag{4}$$

Thus, S can be calculated by determining Q_{ratio} without calculating the exact amount of excess hole density and the effect of bulk recombination. The τ_s value was also calculated by μ-PCD using the following well-known equation to confirm the reliability of the S value [37]:

$$S = \frac{WD\pi^2}{2\left(D\pi^2\tau_s - W^2\right)}, \tag{5}$$

where W is the thickness of the Si substrate and D is the minority carrier diffusion constant of n-Si.

3 Results and discussion

3.1 Solution-processed TiO_2

Figure 3a shows the AFM image and line profile of 2-nm-thick TiO_2 spin coated from the precursor with 1 mg/ml concentration on an n-Si wafer. The RMS value was 0.215 nm in the $5 \times 5\ \mu m^2$ area, which value was almost same with that of ALD. In Figure 3b, the 2-dimensional map of τ_s is shown for 2- and 10-nm-thick TiO_2. About 4 times higher average lifetime value was observed for the ~2-nm-thick TiO_2 coated device compared to the bare-Si (~7 μs), with slight non-uniformity, this non-uniformity may come from partial Si surface exposure to air due to the ultrathin TiO_2 layer. The ~10 nm-thick-TiO_2 coated sample shows comparatively uniform and 5~6 times higher lifetime value with respect to bare silicon. Although these lifetime values are much lower than the PEDOT:PSS value (~230 μs) (Fig. 3c), which implies that the passivation level was worse compared to the PEDOT:PSS/n-Si anode interface. Thus, recombination properties of PEDOT:PSS/n-Si/TiO_2 structure is mostly dominated by cathode (Si/TiO_2) interface.

3.2 Photovoltaic performance of solar cells

Figure 4a shows the J–V characteristics of PEDOT:PSS/n-Si heterojunction solar cells with different thickness TiO_2 HBLs of 1, 2, and 3 nm, together with that of a pristine (without TiO_2) device under AM1.5G simulated solar light exposure. The solar cell parameters for the corresponding devices are summarized in Table 1. J_{sc} increased from 27.53 to 30 mA/cm^2 with increasing FF and V_{oc} for TiO_2 thicknesses of 1 and 2 nm. This is due to the lowering of the work function of Al by inserting a TiO_2 layer as well as the enhanced hole blocking capability at the cathode interface. A large number of holes diffuse backward inside the bulk Si. As a result, the PCE increased from 11.23% for the pristine device to 13.08% for a TiO_2 HBL device on a plain substrate with a TiO_2 thickness of ~2 nm.

Figure 4b presents the EQE for PEDOT:PSS/n-Si devices with and without a 2-nm-thick TiO_2 HBL double layer. The inset shows the normalized EQE of the corresponding device. The EQE at the n-Si/cathode interface region corresponding to a wavelength of ~1000 nm increased for the double-layer TiO_2 inserted device more than for the single-layer device. These findings originate from the reduction of carrier recombination at the Si/cathode interface. In addition, electroluminescence images at the far infrared region due to dark current injection from the cathode interface for the devises are compared (Fig. 4c). The emission image is more intense for

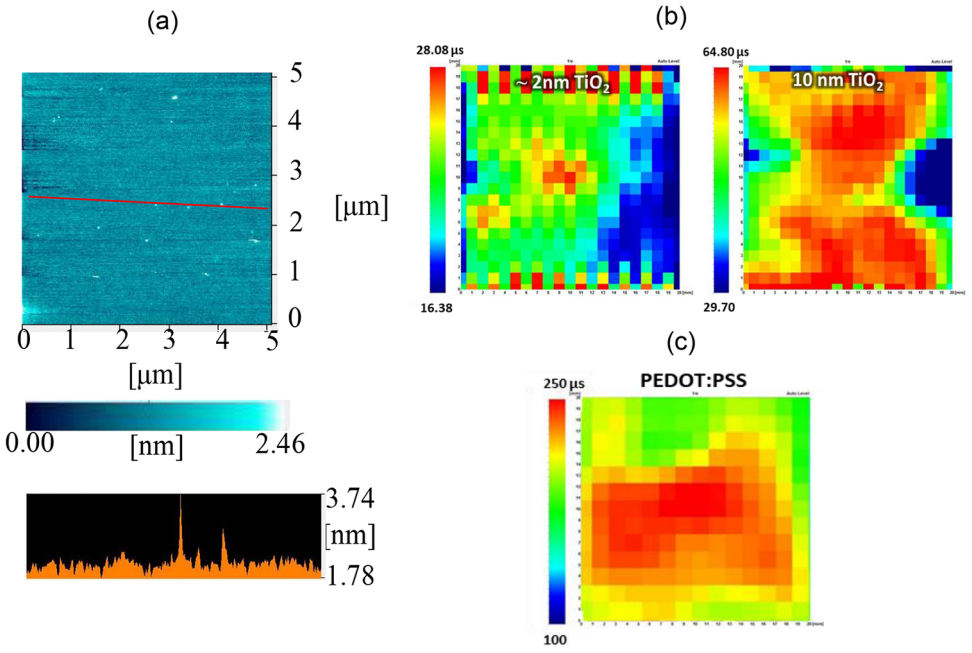

Fig. 3. (a) AFM image and line profile for 2-nm-thick TiO_2 on an n-Si wafer. (b) 2D map of τ_s for 2- and 10-nm-thick TiO_2 coated on n-Si at both the front and bottom surfaces. (c) 2D map of τ_s for 80-nm-thick PEDOT:PSS.

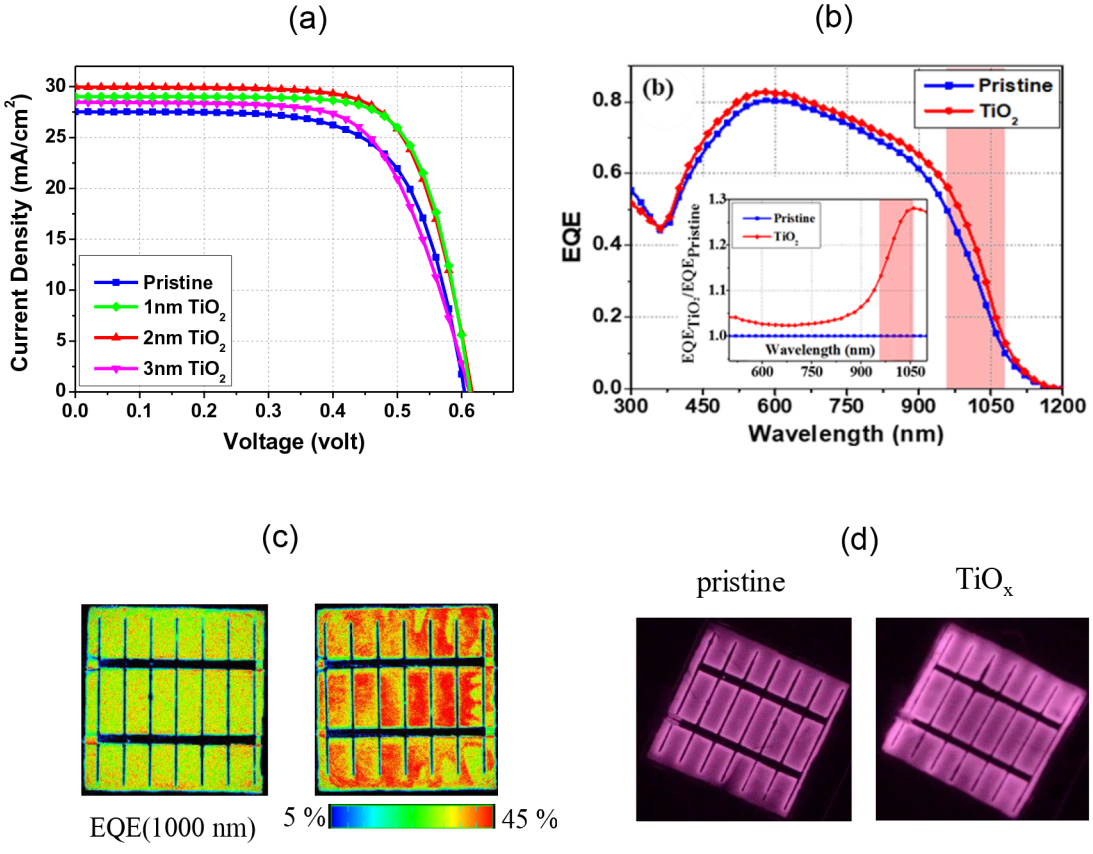

Fig. 4. (a) *J–V* curve of PEDOT:PSS/n-Si solar cells TiO_2 HBLs with different layer thicknesses. (b) EQE for devices with and without a 2-nm-thick TiO_2 HBLs. The inset shows $EQE_{TiO2}/EQE_{pristine}$. (c) 2D map of EQE at 1000 nm and (d) far-infrared EL emission images for devices with and without a 2-nm-thick TiO_2 HBL.

Table 1. Solar cell parameters, J_{sc}, V_{oc}, FF, and PCE of PEDOT:PSS/n-Si solar cells with of TiO_2 HBLs of various thicknesses.

Device type		J_{sc} (mA/cm^2)	V_{oc} (mV)	FF (%)	PCE (%)
Pristine		27.5	605	68.0	11.23
TiO_2	1 nm	29.0	613	73.1	13.01
	2 nm	30.0	616	70.9	13.08
	3 nm	28.5	612	65.8	11.46

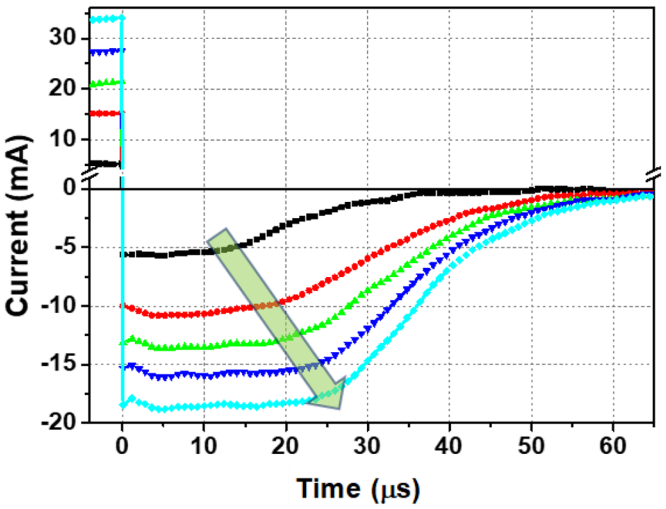

Fig. 5. T_{rr} current for a PEDOT:PSS/n-Si heterojunction solar cell with different forward currents.

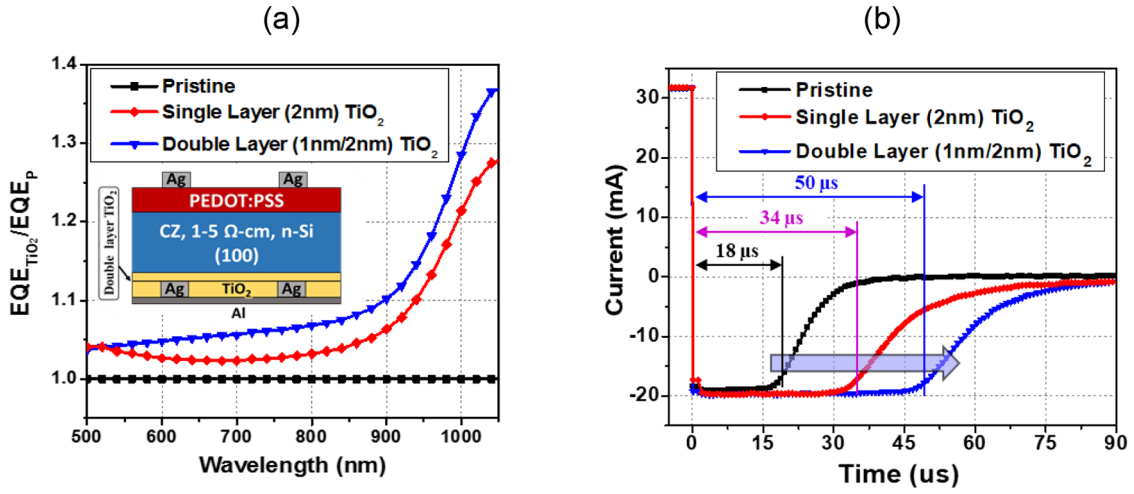

Fig. 6. (a) Normalized EQE, $EQE_{TiO2}/EQE_{pristine}$ and (b) T_{rr} current profiles of PEDOT:PSS/n-Si heterojunction solar cells with single- and double-layer of 2-nm-thick TiO_2 HBLs including the recovery time for each devices.

the device with a TiO_2 HBL than that without an insert HBL, suggesting the increased electron injection from the cathode by a TiO_2 HBL.

3.3 Junction property at Si/TiO_2 cathode interface monitored by T_{rr} characterization

Figure 5 shows the T_{rr} current of a PEDOT:PSS/n-Si/Ag (Al) solar cell with different injection current (forward) levels. The T_{rr} current increased with increasing forward current level together with an extended recovery time. This is because the number of diffused minority carriers (hole) pushed out from PEDOT:PSS to the bulk n-Si is higher for higher injection currents. Thus, the T_{rr} study monitors the diffused (from PEDOT:PSS) minority carrier (hole) inside the bulk n-Si blocked at the cathode interface.

Figure 6b shows the T_{rr} current of PEDOT:PSS/n-Si heterojunction solar cells with 2-nm-thick single- and double-layer TiO_2, as shown in Figure 1b. The hole storage time is ~2 and 2.8 times longer for single- and double-layer devices, respectively, compared to the pristine device without a TiO_2 layer. The amount of stored charge is calculated by multiplying the corresponding t_s with the maximum transient reverse current. An S of ~750 cm/s is obtained for the single-layer TiO_2 inserted device, in which a 15.5% back area of the Si surface is in direct contact with metal (Ag). This value is in a good agreement with the S value measured by conventional μ-PCD. An S value of ~375 cm/s was obtained for the device with a coating alternating of TiO_2 layers (Fig. 1b). To understand the reliability of this value obtained from the T_{rr}, a μ-PCD measurement was performed using PEDOT:PSS and TiO_2 coated n-Si samples at both front and rear sides of c-Si substrate. The S of ~700 cm/s and ~60 cm/s were obtained

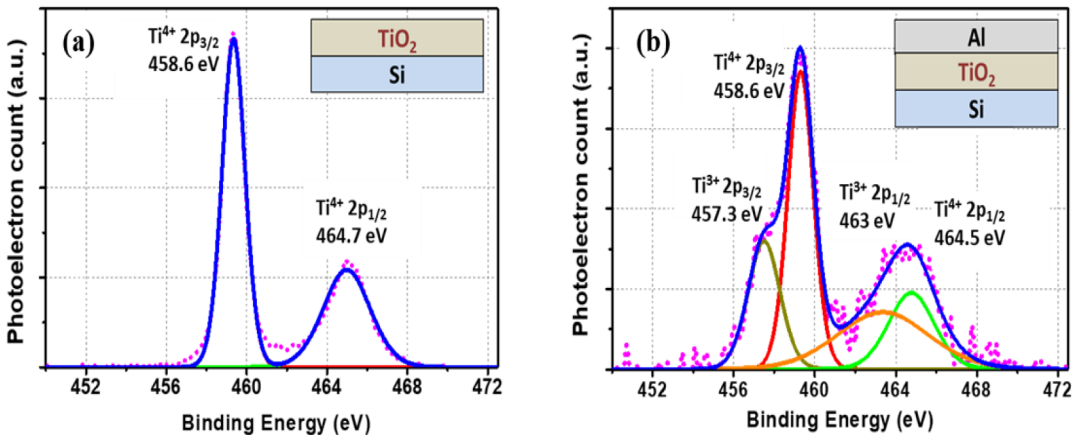

Fig. 7. XPS Ti(2p) core energy region of solution-processed TiO_2 on n-Si (a) before and (b) after Al metallization.

from both sides of the TiO_2 (2 nm) and PEDOT:PSS (80 nm) coated n-Si (1–5 Ω cm) substrates respectively, which suggest that the photovoltaic performance is largely determined by the cathode interface.

However, these S values of the TiO_2 HBL devices are still higher than for PE-CVD SiN_x or a-Si devices. This is because the thinner TiO_2 of ∼2 nm reacts with the underlying TiO_2 during the Al metallization. Figures 7a and 7b show the XPS Ti(2p) core energy region of TiO_2 on n-Si before and after Al metallization. Compared to the spectrum of pristine TiO_2, two additional peaks at 457.3 eV and 463 eV appeared, which originated from the Ti^{3+} oxidation state. These findings suggest that TiO_2 react with the Al during the evaporation and forms a Ti-O-Al complex oxide, which degrades the hole-blocking ability and passivation quality of the TiO_2 layer.

4 Summary and conclusions

The junction properties at the solution-processed TiO_2/n-Si interface were studied using PEDOT:PSS/n-Si heterojunction solar cells. A PCE of 13.08% was obtained for PEDOT:PSS/n-Si/TiO_2 double heterojunction solar cells by adjusting the TiO_2 layer thickness at the n-Si/Ag interface with increased J_{sc} and V_{oc}. These findings originate from the efficient carrier collection at the n-Si/cathode interface, although surface recombination at the cathode interface dominate the photovoltaic performance. Trr provides the S value using the solar cell device structures with no need to examine both sides of TiO_2 coated c-Si.

This study was supported in part by the Ministry of Education, Culture, Sports, Science and Technology (MEXT) and the Takahashi Industrial and Economic Research Foundation.

Author contribution statement

All authors contributed equally to this work.

References

1. A.S. Erickson, A. Zohar, D. Cahen, Adv. Ener. Mater. **4**, 1301724 (2014)
2. S. Jäckle, M. Mattiza, M. Liebhaber, G. Brönstrup, M. Rommel, K. Lips, S. Christiansen, Sci. Rep. **5**, 13008 (2015)
3. A.T.M. Saiful Islam, R. Ishikawa, H. Shirai, *Advanced Nanomaterials for Solar Cells and Light Emitting Diodes*, 1st edn. (Elsevier, 2019), pp. 97–117
4. T.G. Allen, J. Bullock, Q. Jeangros, C. Samundsett, Y. Wan, J. Cui, A. Hessler-Wyser, S. De Wolf, A. Javey, A. Cuevas, Adv. Energy Mater. **7**, 1602606 (2017)
5. Y. Wan, C. Samundsett, D. Yan, T. Allen, J. Peng, J. Cui, X. Zhang, J. Bullock, A. Cuevas, Appl. Phys. Lett. **109**, 113901 (2016)
6. P.L. Janega, J. McCaffrey, D. Landheer, M. Buchanan, M. Denhoff, D. Mitchel, Appl. Phys. Lett. **53**, 2056 (1988)
7. Y. Wan, C. Samundsett, J. Bullock, M. Hettick, T. Allen, D. Yan, J. Peng, Y. Wu, J. Cui, A. Javey, A. Cuevas, Adv. Energy Mater. **7**, 1601863 (2017)
8. X. Yang, P. Zheng, Q. Bi, K. Weber, Sol. Energy Mater. Sol. Cells **150**, 32 (2016)
9. K.A. Nagamatsu, S. Avasthi, G. Sahasrabudhe, G. Man, J. Jhaveri, A.H. Berg, J. Schwartz, A. Kahn, S. Wagner, J.C. Sturm, Appl. Phys. Lett. **106**, 123906 (2015)
10. S. Avasthi, W.E. McClain, G. Man, A. Kahn, J. Schwartz, J.C. Sturm, Appl. Phys. Lett. **102**, 203901 (2013)
11. J. He, Z. Ling, P. Gao, J. Ye, Sol. RRL **1**, 1700154 (2017)
12. J. Jhaveri, K.A. Nagamatsu, A.H. Berg, G. Man, G. Sahasrabudhe, S. Wagner, J. Schwartz, A. Kahn, J.C. Sturm, in *2015 IEEE 42nd Photovolt. Spec. Conf. PVSC* (IEEE, 2015), https://doi.org/10.1109/PVSC.2015.7356054
13. P.J. Cameron, L.M. Peter, J. Phys. Chem. B **107**, 14394 (2003)
14. J. Hossain, K. Kasahara, D. Harada, A.T.M. Saiful Islam, R. Ishikawa, K. Ueno, T. Hanajiri, Y. Nakajima, Y. Fujii, M. Tokuda, H. Shirai, J. Appl. Phys. **122**, 55101 (2017)
15. A.T.M.S. Islam, M.E. Karim, A. Rajib, Y. Nasuno, T. Ukai, S. Kurosu, M. Tokuda, Y. Fujii, Y. Nakajima, T. Hanajiri, H. Shirai, Appl. Phys. Lett. **114**, 193901 (2019)
16. Y. Zhang, W. Cui, Y. Zhu, F. Zu, L. Liao, S.T. Lee, B. Sun, Energy Environ. Sci. **8**, 297 (2015)

17. W. Wu, J. Bao, X. Jia, D. Liu, L. Cai, B. Liu, J. Song, H. Shen, Phys. Status Solidi − Rapid Res. Lett. **10**, 662 (2016)
18. J. Bullock, M. Hettick, J. Geissbühler, A.J. Ong, T. Allen, C.M. Sutter-Fella, T. Chen, H. Ota, E.W. Schaler, S. De Wolf, C. Ballif, A. Cuevas, A. Javey, Nat. Energy **1**, 15031 (2016)
19. J. Bullock, P. Zheng, Q. Jeangros, M. Tosun, M. Hettick, C.M. Sutter-Fella, Y. Wan, T. Allen, D. Yan, D. Macdonald, S. De Wolf, A. Hessler-Wyser, A. Cuevas, A. Javey, Adv. Energy Mater. **6**, 1600241 (2016)
20. Y. Wan, C. Samundsett, J. Bullock, T. Allen, M. Hettick, D. Yan, P. Zheng, X. Zhang, J. Cui, J. McKeon, A. Javey, A. Cuevas, ACS Appl. Mater. Interfaces **8**, 14671 (2016)
21. H.J. Frenck, W. Kulisch, M. Kuhr, R. Kassing, Thin Solid Films **201**, 327 (1991)
22. W.G. Lee, S.I. Woo, J.C. Kim, S.H. Choi, K.H. Oh, Thin Solid Films **237**, 105 (1994)
23. W. Yang, C.A. Wolden, Thin Solid Films **515**, 1708 (2006)
24. D. Li, M. Carette, A. Granier, J.P. Landesman, A. Goullet, Appl. Surf. Sci. **283**, 234 (2013)
25. K.L. Ou, D. Tadytin, K. Xerxes Steirer, D. Placencia, M. Nguyen, P. Lee, N.R. Armstrong, J. Mater. Chem. A **1**, 6794 (2013)
26. M.F. Brunella, M. V Diamanti, M.P. Pedeferri, F. Di Fonzo, C.S. Casari, A.L. Bassi, Thin Solid Films **515**, 6309 (2007)
27. R. Methaapanon, S.F. Bent, J. Phys. Chem. C **114**, 10498 (2010)
28. J. Dendooven, S. Pulinthanathu Sree, K. De Keyser, D. Deduytsche, J.A. Martens, K.F. Ludwig, C. Detavernier, J. Phys. Chem. C **115**, 6605 (2011)
29. S. McDonnell, R.C. Longo, O. Seitz, J.B. Ballard, G. Mordi, D. Dick, J.H.G. Owen, J.N. Randall, J. Kim, Y.J. Chabal, K. Cho, R.M. Wallace, J. Phys. Chem. C **117**, 20250 (2013)
30. L. Tian, A. Soum-Glaude, F. Volpi, L. Salvo, G. Berthomé, S. Coindeau, A. Mantoux, R. Boichot, S. Lay, V. Brizé, E. Blanquet, G. Giusti, D. Bellet, J. Vac. Sci. Technol. A **33**, 01A141 (2015)
31. J. Kischkat, S. Peters, B. Gruska, M. Semtsiv, M. Chashnikova, M. Klinkmüller, O. Fedosenko, S. Machulik, A. Aleksandrova, G. Monastyrskyi, Y. Flores, W.T. Masselink, Appl. Opt. **51**, 6789 (2012)
32. L.-L. Yang, Y.-S. Lai, J. S. Chen, P. H. Tsai, C.L. Chen, C.J. Chang, J. Mater. Res. **20**, 3141 (2005)
33. B. Hoex, J. Schmidt, P. Pohl, M.C.M. van de Sanden, W.M.M. Kessels, J. Appl. Phys. **104**, 044903 (2008)
34. D.A.H. Hanaor, I. Chironi, I. Karatchevtseva, G. Triani, C.C. Sorrell, Adv. Appl. Ceram. **111**, 149 (2012)
35. K.A. Nagamatsu, S. Avashi, G. Sahasrabudhe, G. Man, J.J. haveri, A.H. Berg, J. Schwartz, A. Kahn, S. Wagner, J.C. Sturm, Appl. Phys. Lett. **106**, 123906 (2015)
36. A.H. Berg, K.A. Nagamatsu, J.C. Sturm, IEEE Trans. Electr. Dev. **64** (2017)
37. D.K. Schroder, in *Semiconductor Materilas and Device Charactrization* (John Wiley & Sons, NewYork, 1990), p. 359

Cite this article as: Md. Enamul Karim, A.T.M. Saiful Islam, Yuki Nasuno, Abdul Kuddus, Ryo Ishikawa, Hajime Shirai, Solution-processed TiO_2 as a hole blocking layer in PEDOT:PSS/n-Si heterojunction solar cells, EPJ Photovoltaics **11**, 7 (2020)